Materials Horizons

Enthalpy-Uphill Exciton Dissociation at Organic/2D Heterostructures Promotes Free Carrier Generation

Journal:	*Materials Horizons*
Manuscript ID	MH-COM-09-2023-001522.R1
Article Type:	Communication
Date Submitted by the Author:	08-Nov-2023
Complete List of Authors:	Rudayni, Fatimah; University of Kansas College of Liberal Arts and Sciences, Department of Physics and Astronomy Rijal, Kushal; University of Kansas College of Liberal Arts and Sciences, Department of Physics and Astronomy Fuller, Neno; University of Kansas College of Liberal Arts and Sciences, Department of Physics and Astronomy Chan, Wai-Lun; University of Kansas College of Liberal Arts and Sciences, Department of Physics and Astronomy

New concepts

Hot excited electronic states typically lose their energy to the environment on the femto- and pico-seconds timescales – a process generally known as the hot electron cooling. In this work, it is found that the CT exciton at organic/2D heterostructures can violate this general behavior by gaining energy from the environment and dissociating spontaneously into an electron-hole pair. We hypothesize that the observed enthalpy-uphill process is driven by entropic gain. While the entropic driving force is often neglected, it would hold the key in facilitating the conversion of bound excitons into free carriers and prolonging the free carrier lifetime. Dissociation of bound excitons into free carriers is a critical step for many photo-to-electrical and photo-to-chemical energy conversion processes. Hence, understanding how to exploit entropy is essential for designing nano-structured materials for harvesting solar energy.

Enthalpy-Uphill Exciton Dissociation at Organic/2D Heterostructures Promotes Free Carrier Generation

Fatimah Rudayni,[1,2] Kushal Rijal,[1] Neno Fuller,[1] Wai-Lun Chan[1,*]

1. Department of Physics and Astronomy, University of Kansas, Lawrence, Kansas 66045, US

2. Department of Physics, Jazan University, Jazan 45142, Saudi Arabia

Abstract

Despite the large binding energy of charge transfer (CT) excitons at type-II organic/2D heterostructures, it has been demonstrated that free carriers can be generated from CT excitons with a long lifetime. Using a model fluorinated zine phthalocyanine (F_8ZnPc)/monolayer-WS_2 interface, we find that CT excitons can dissociate spontaneously into free carriers despite it is an enthalpy-uphill process. Specifically, it is observed that CT excitons can gain an energy of 250 meV in 50 ps and dissociate into free carriers without any applied electric field. This observation is surprising because excited electrons typically lose energy to the environment and relax to lower energy states. We hypothesize that this anormal enthalpy-uphill CT exciton dissociation process is driven by entropy gain. Kinetically, the entropic driving force can also reduce the rate for the reverse process – the conversion of free electron-hole pairs back to CT excitons. Hence, this mechanism can potentially explain the very long carrier lifetime observed at organic/2D heterostructures.

*wlchan@ku.edu

Introduction

Two-dimensional (2D) crystals such as graphene and transition metal dichalcogenide crystals (TMDCs) have attracted much attention recently because their properties can be tailored by stacking different atomically thin crystals together.[1-3] This fabrication strategy is feasible because of the weak van der Waals (vdW) bonding between layers and the absence of dangling bonds at the interface. Similarly, organic molecules, when physically absorbed on TMDCs, interact with the substrate by vdW forces. Hence, organic molecules can be naturally combined with TMDCs to produce heterostructures that possess advantages of both materials.[4-6] For example, organic molecules are tunable light absorbers, and the thickness of an organic film can be easily controlled. They can be combined with TMDCs to produce sensitive light detectors and gate-tunable p-n junctions.[7-12] It has been demonstrated that these p-n junctions can have a dimension on the atomic scale.[13] Organic molecules can also passivate defects in TMDCs *via* physical adsorption[14] which is important for improving the carrier mobility in TMDCs. In some cases, organic molecules can enhance the photoluminescence yield of TMDCs by effective energy transfer.[15, 16] An array of molecules can be used to create periodic exciton trapping sites at organic/TMDC interfaces,[17] which can favor the formation of exciton condensates.[18] Molecules can also be attached to TMDCs *via* covalent bond, which allows the use of these heterostructures in solution environments.[19]

In type-II vdW heterostructures, electrons and holes can transfer into the two different layers because of the staggered band gap at the interface. Although the electron and hole reside in two different layers, they can still be bound together by Coulomb interaction to form an exciton, which is also known as a charge transfer (CT) exciton. CT excitons usually form immediately after photoexcitation,[20, 21] and they typically have a very long lifetime.[22] These properties are beneficial

for optoelectronic and light harvesting applications. On the other hand, because of the large exciton binding energy, it is not guaranteed that free carriers can be generated from these bound excitons, which can hamper the use of these heterostructures in light harvesting and sensing applications. Indeed, it is known that the dissociation of CT excitons can be a bottleneck process for free carrier generation,[23, 24] and the large binding energy of CT excitons has been shown to limit the open circuit voltage of organic photovoltaics (OPV).[25, 26]

Interestingly, the carrier lifetime at molecule/TMDC heterostructures has shown to be an order of magnitude larger than that at TMDC/TMDC heterostructures.[27-29] While a thicker organic layer generally helps by allowing free carriers to diffuse away from the interface, it is less clear how bound CT excitons would dissociate in the first place. Because organic films often have a smaller dielectric constant compared to TMDCs, the CT exciton at the molecule/TMDC can have a binding energy as large as ~0.5 eV,[18] which should impede its dissociation. If CT excitons are less likely to dissociate into free carriers, free carriers can also be trapped at the interface by forming CT excitons. Therefore, the much longer carrier lifetime observed in molecule/TMDC heterostructures can be counterintuitive because the lifetime of free carriers should be lowered if they have a higher tendency to meet their counterpart to form CT excitons. To resolve this dilemma, we use time-resolved two photon photoemission spectroscopy (TR-TPPE) to probe the CT exciton dissociation process at fluorinated zinc phthalocyanine (F_8ZnPc)/WS_2 heterostructure. This method can distinguish bound CT excitons from free carriers by their energies,[30, 31] which allows us to probe how the charge separation (CS) process occurs.

Although observations of free carrier generation from similar interfaces have been reported in several previous works,[32-35] these works have not resolved whether the CS state has a higher energy than the CT exciton. Indeed, many earlier studies on organic interfaces have suggested that

effective CS relies on the extraction of electrons from CT excitons *via* some lower energy sites originated from interfacial mixing[36, 37] or disorders.[38] In our previous TR-TPPE study on ZnPc/MoS_2,[35] we observed the ultrafast electron transfer from ZnPc into MoS_2. However, because our probe photons do not have a high enough energy to access the free carrier state in the MoS_2,[39] we were only able probe the localized CT state but not the CS state. The presence of the CS can only be inferred from complementary transient absorption measurements.[35] In this work, a F_8ZnPc/WS_2 heterostructure is chosen such that the electron in the CT exciton resides in the molecule instead of the TMDC. This sample geometry, with the organic layer on the top, also allows us to probe the electron in the CT exciton with the surface sensitive photoemission probe even for heterostructures with a thicker organic layer. Finally, the F_8ZnPc has a smaller ionization potential compared to typical electron acceptor molecules, which enables us to probe the full manifold of S_1, CT and CS states with our laser setup.

Surprisingly, instead of electron trapping at the interface, we found that bound CT excitons at the F_8ZnPc/WS_2 heterostructure can gain an energy of ~0.25 eV in just 50 ps, which allows free carrier generation to occur spontaneously despite being an enthalpy-uphill process. Because no electric field is applied during the measurement, it is rather unexpected that a higher energy state can be populated at the expense of a lower energy state. We attribute this anormal enthalpy-uphill process to entropy-driven CT exciton dissociation. We have observed similar phenomena at organic donor/acceptor interfaces,[30, 40] but it is the first time that this process has been reported at hybrid organic/TMDC interfaces. The significance of observing this phenomenon at organic/TMDC interfaces is two-fold. First, it can explain why the CS in organic/TMDC heterostructures appears to be more effective than that in TMDC/TMDC heterostructures despite CT excitons in the former should have a larger binding energy. Second, it validates our earlier

hypothesis that entropy-driven CS is favored at interfaces in which the delocalized electron and hole wavefunctions within the CT exciton have minimal spatial contact.[30, 40] As we will elaborate later, a large enough entropic driving force not only means that CT excitons are more likely to dissociate, but it also suppresses the reverse process, i.e., the conversion of free carriers back to CT excitons. This mechanism can explain the long carrier lifetime observed at organic/2D heterostructures.[27-29]

Results and discussion

A type-II heterostructures is formed by depositing F_8ZnPc molecules on a continuous CVD-grown monolayer (ML) WS_2 in an ultrahigh vacuum (UHV) chamber. A schematic diagram of the sample is shown in Fig. 1a. Our previous optical spectroscopy work has shown that this heterostructure can generate separated electrons and holes effectively.[32] The detailed sample preparation procedure can be found in the method section. Before the deposition, the ML-WS_2 was annealed at 400 – 450 ^{0}C for ~ 30 hours, which was then characterized *in-situ* by angle-resolved photoemission spectroscopy (ARPES). The ARPES spectrum (Fig. 1b) shows a clear dispersion relationship that agrees well with previous works.[41] We note that the WS_2 is polycrystalline, with a grain size of ~100 μm. The grain size is large enough that the exciton dynamics and the band structure obtained in our work should be comparable to measurements performed on exfoliated flakes. However, because the UV light used in our ARPES measurement is not focus, the ARPES spectrum represents the band structure averaged over grains in a few mm^2 area that can have different azimuthal directions. After obtaining a clean WS_2 surface, F_8ZnPc was deposited on the WS_2.

The ultraviolet photoemission spectra (UPS) of the sample with various F_8ZnPc thicknesses measured at the surface normal direction, corresponding to the Γ point, are shown in

Fig. 1c. The initial state energy is referenced with respect to the Fermi level (E_f). The valence band maximum (VBM) at the Γ point of WS_2 and the highest occupied molecular orbital (HOMO) of F_8ZnPc can be identified in these spectra. The secondary electron cutoff (SECO) at low energies (Fig. S1 in ESI) was used to determine the work function of the sample. The HOMO peak position and the work function of the F_8ZnPc are plotted in Fig. 1d. Both quantities change slightly as the thickness of the F_8ZnPc layer increases. The ionization potential (IP) of F_8ZnPc can also be determined from the UPS spectrum by using the SECO and the rising edge of the HOMO peak (Fig. S2 in ESI). The IP as a function of thickness is shown in Fig. 1e. The IP converges to ~ 5.9 eV for thicknesses > 10 nm.

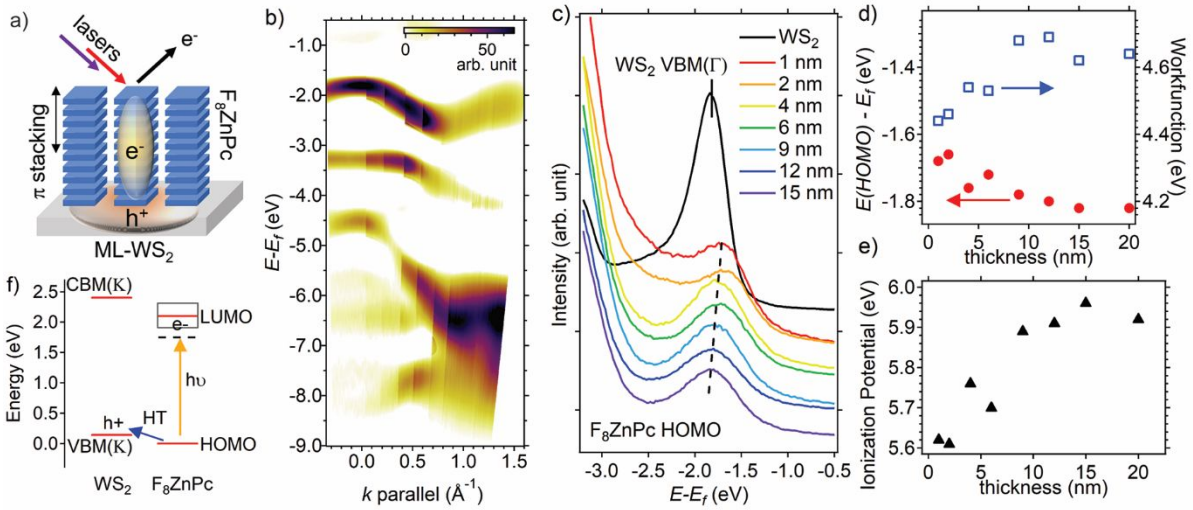

Figure 1: a) A schematic showing the F_8ZnPc/ML-WS_2 heterostructure. b) The ARPES spectrum for the ML-WS_2. The pseudocolor represents the second derivative of the intensity with respect to the energy. c) The UPS spectra for the bare ML-WS_2 and F_8ZnPc films on ML-WS_2. The nominal thickness of the F_8ZnPc film is shown in the legend. The spectra are collected with photoelectrons emitted in the surface normal direction. d) The HOMO peak position and the work function of the F_8ZnPc as a function of the film thickness. e) The ionization potential of the F_8ZnPc film. f) The band diagram of the F_8ZnPc/ML-WS_2 heterostructure drawn by using the measured HOMO-VBM offset and quasiparticle band gaps of ML-WS_2 and F_8ZnPc.

For small molecules, the IP of thicker films (when the substrate effect is less important) depends on the surface dipole, which in turns depends on the orientation of the molecule.[42, 43] For

phthalocyanine molecules, these effects have been well-studied.[40, 43-45] For instance, it is known that face-on oriented ZnPc (or other metal-Pcs) have a IP that is ~ 0.4 eV larger than that of edge-on oriented ZnPc.[43-45] The effect is reversed for F_8ZnPc, i.e., the IP for face-on orientated F_8ZnPc is ~ 0.3 - 0.4 eV smaller than that of edge-on F_8ZnPc,[40, 45] because electropositive H atoms on the edge of the molecule are replaced by electronegative F atoms. In this work, the measured IP value (5.9 eV) agrees well with the IP of face-on orientated F_8ZnPc (in our previous work,[40] we found that face-on and edge-on F_8ZnPc has an IP of 5.9 eV and 6.2 eV, respectively). If we used the peak position instead of the rising edge to determine the IP, we found an IP value of 6.46 eV, which agrees well with the IP value of face-on F_8ZnPc (~6.5 eV) determined by others using the peak position.[45] The face-on orientation is also consistent with at least two other near-edge X-ray absorption spectroscopy works, which found F-CuPc[46] and F-FePc[33] molecules adopted a face-on orientation on MoS_2.

The band alignment at the interface is determined by the relative position of the WS_2-VBM(Γ) peak and the F_8ZnPc-HOMO peak shown in Fig. 1c. We note that the global VBM for ML-WS_2 is at the K point, which cannot be measured directly from a polycrystalline sample. For ML-WS_2, the VBM at the K point is 0.3 eV higher than that at the Γ point,[41] which is added to the VBM(Γ) to determine the VBM(K). For F_8ZnPc, the average HOMO energy for the two thinnest samples (1 nm, 2 nm) is used, which corresponds to the HOMO energy near the interface. These energy levels are plotted in Fig. 1f. In this diagram, the HOMO level is set at 0 eV. In order to determine the position of the conduction band minimum (CBM) and the lowest unoccupied molecular orbital (LUMO), reported bandgaps of these materials are used. We note that both materials have a large exciton binding energy. For ML-WS_2, the quasiparticle band gap is determined by adding an exciton binding energy of 0.23 eV[47] to the optical bandgap of 2.03 eV.

We could not find the quasiparticle band gap for F_8ZnPc in the literature. For similar phthalocyanine molecules, the reported transport gap is in the range of 1.9-2.3 eV.[48-50] Hence, a value of 2.1 eV is used in the band diagram. As shown in the diagram, the heterostructure has a type-II band alignment. We note that the HOMO energy decreases as the F_8ZnPc thickness increases, which can further increase the HOMO-VBM(K) offset and reinforce the type-II alignment. We also show the uncertainty (±0.2 eV) in the transport gap of F_8ZnPc in Fig. 1f (the gray box). Including this uncertainty does not affect the overall type-II band alignment.

For the TR-TPPE measurement, the heterostructure was pumped by 1.77 eV, 25 fs laser pulses. The pump pulses selectively excite F_8ZnPc because the pump photon energy is smaller than the optical gap of ML-WS_2. Then, time-delayed 4.68 eV, 65 fs probe pulses were used to ionize the excited electrons. The kinetic energy of photoelectrons was measured by an electron spectrometer to produce the TPPE spectrum. We note that laser pulses/photoelectrons are illuminated/detected on the F_8ZnPc side. The TPPE spectra at different delay times for the 1-nm F_8ZnPc/WS_2 are shown in Fig. 2a as a 2D pseudo color plot. We note that at each delay time, the raw spectrum is subtracted by the background spectrum obtained at negative delay times. Hence, the signal in the spectrum is originated from excited states populated by the pump pulse. The intermediate state (excited state) energy is referenced with respect to the F_8ZnPc-HOMO energy obtained by the UPS (Fig. S3 in ESI). At the time-zero, the F_8ZnPc is first optically excited. Hence, the peak at ~ 1.6 eV in early times (< 0.5 ps) can be attributed to the singlet exciton (S_1) of F_8ZnPc. This energy is also consistent with the S_1 energy of phthalocyanine films measured by luminescence spectroscopy.[51] The spectral narrowing in the first 0.2 ps can be attributed to exciton localization.[52]

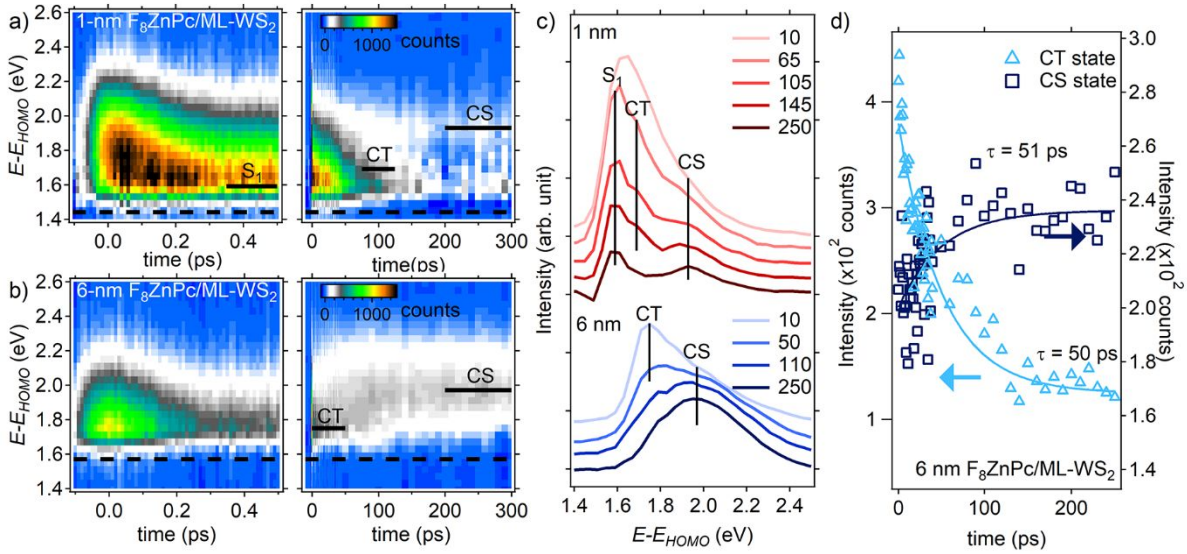

Figure 2: The TR-TPPE spectra for the a) 1-nm F_8ZnPc/ML-WS_2, and b) 6-nm F_8ZnPC/ML-WS_2 sample on two different timescales. The intermediate state energy is referenced with respect to the F_8ZnPc's HOMO. Peaks correspond to the F_8ZnPc-S_1 exciton, the CT exciton, and the CS state are labeled. The horizontal dashed line in each plot represents the lowest electronic energy that can be probed by 4.68 eV photons. c) The TPPE spectra at different delay times for the two samples. In this plot, spectra are offset vertically for clarity. Each curve represents the averaged spectrum over a time window of 30 ps, except for the 10 ps curve, which is averaged over the period of 5 - 15 ps. The center of each time window is shown in the legend. d) The intensity of the CT and CS peak as a function of time for the 6-nm F_8ZnPc/ML-WS_2 sample. The CT (CS) intensity is fit with an exponential decay(rise) function. For both curves, a time constant of ~ 50 ps is obtained from the fit.

At longer times (> 10 ps), the spectrum is sharpened, and two additional higher energy peaks can be resolved. These higher energy peaks can be seen more clearly by plotting the spectra at various delay times (Fig. 2c, upper panel). The two higher energy peaks at ~ 1.7 eV and ~ 1.95 eV are assigned to the CT state and the charge separated (CS) state, respectively. The CT exciton can be produced by the hole transfer from F_8ZnPc to WS_2 (blue arrow in Fig. 1f). A higher photoelectron energy of the CT peak as compared to the S_1 peak can be explained by a reduction in the exciton binding energy. To determine the CT exciton energy in our spectrum, we need to subtract the peak position (~1.7 eV) by the VBM-HOMO offset. This is because the energy on the TPPE spectrum is referenced with respect to the F_8ZnPc's HOMO and the hole in the CT exciton

locates at the WS_2's VBM. From our UPS data, the VBM-HOMO offset is ~0.14 eV, which gives a CT exciton energy of ~1.56 eV. As the CT exciton dissociates, the CT exciton binding energy decreases, which can result in the production of the higher energy CS state. The assigned CS peak is at ~ 0.25 eV higher than the CT peak. The energy difference between the CT and CS peaks represents the binding energy of the CT exciton. The CS peak is located at ~ 1.9 – 2.0 eV above the F_8ZnPc's HOMO, which agrees well with the HOMO-LUMO gap reported for phthalocyanine molecules (1.9-2.3 eV.[48-50]). At t > 200 ps, the S_1 peak and the CS peak becomes the two most dominate features in the spectrum, which indicates that the exciton either dissociates or remains as a S_1 exciton in the F_8ZnPc.

The dissociation of CT exciton into the CS state is more visible with a thicker F_8ZnPc layer. Figure 2b shows the TR -TPPE spectrum for a 6 nm-F_8ZnPc/ML-WS_2 sample. Again, for t < 0.5 ps, a peak corresponds to the F_8ZnPc S_1 can be observed. We note that because of the larger work function and the deeper HOMO level of the thicker F_8ZnPc film (see Fig. 1d), our 4.68 eV probe pulse does not have enough energy to capture the full S_1 peak (the horizontal dashed line in Fig. 2b indicates the lowest energy that we can measure based on the work function and the probe photon energy). Since the TPPE spectrum only captures the high energy tail of the S_1 peak, the intensity appears to decay rapidly as the hot S_1 exciton relaxes in the first 0.2 ps. Nevertheless, the probe can still capture the energy window corresponding to the CT and CS states (Fig. 2b – right panel, Fig. 2c – bottom panel). At t ~ 10 ps, the CT state, together with the higher energy CS state, are generated. The generation of the CS state within this short timescale can be attributed to hot mechanisms as suggested by a recent work on organic/2D interfaces.[34] For t > 10 ps, the intensity of the CT state decreases as the intensity for the CS state increases. Figure 2d shows the intensity of the two peaks as a function of time. The two curves can be fit independently by an exponential

rise/decay function. Very similar time constants (τ) of 50 ps (CT) and 51 ps (CS) are obtained from the two curves, which indicates that the population is transferred from the lower energy CT state to the higher energy CS state in ~ 50 ps. This population transfer causes an apparent shift in the photoemission peak towards higher energies as a function of time, which can be seen in the TR-TPPE spectrum (Fig. 2b, right panel). We also provide a grayscale version of this 2D intensity map in the ESI (Fig. S4b) in which the shift in the spectral weight can be more apparent. The shift in the spectral weight from the CT to the CS state can also be seen by plotting a series of raw spectra at different delay times, which is shown in Fig. S4a.

We note that the shift in the photoemission peak towards higher energies cannot be explained by a surface photovoltage effect.[53-55] Such effect should be less pronounced at lower pump laser fluences because less electrons and holes are separated.[53, 54] However, we observe an opposite behavior in which the intensity growth of the higher energy CS state is more pronounced at lower fluences (Fig. S5 in ESI). This observation can be explained by the Coulomb repulsion between electrons generated from neighboring CT excitons, which could suppress the charge separation at higher excitation densities. At the highest pump fluence we used, the excitation density is estimated to be ~ 6×10^{12} cm^{-2} (see the experimental section). Moreover, the SECO from the raw TPPE spectra that includes the photoemission background does not show any shift in the energy as a function of time (Fig. S6 in ESI), which indicates that the observed energy upshift is originated from an actual increase in the excited state energy, rather than a transient shift in the work function induced by the photoexcitation.[56]

The energy upshift observed in Fig. 2b is rather atypical. For most materials that we have worked on, the population of lower energy states increases at the expense of the population of higher energy states.[31, 52, 57-60] Indeed, by the principle of detailed balance, if the enthalpy change

(ΔE) is the only contribution to the free energy change (ΔF), the ratio of the concentration of the higher energy CS state to that of the lower energy CT state should be given by $\exp(-\Delta E/k_B T)$, where ΔE is the energy difference between the two states. In our case, $\Delta E \sim 0.25$ eV. Hence, the concentration of the CS state should only be $\sim 5 \times 10^{-5}$ of that of the CT state. This low concentration of the high energy CS state should render it unobservable. Hence, the emergence of the higher energy CS state in the spectrum is quite surprising. Previously, in our works on organic/organic interfaces, we suggested that a population transfer to the higher energy CS state implies that the entropy contribution ($-T\Delta S$) to ΔF cannot be neglected.[30, 40] If the ΔE is largely compensated by $-T\Delta S$, the dissociation of the CT exciton can occur spontaneously despite it is an enthalpy uphill process.

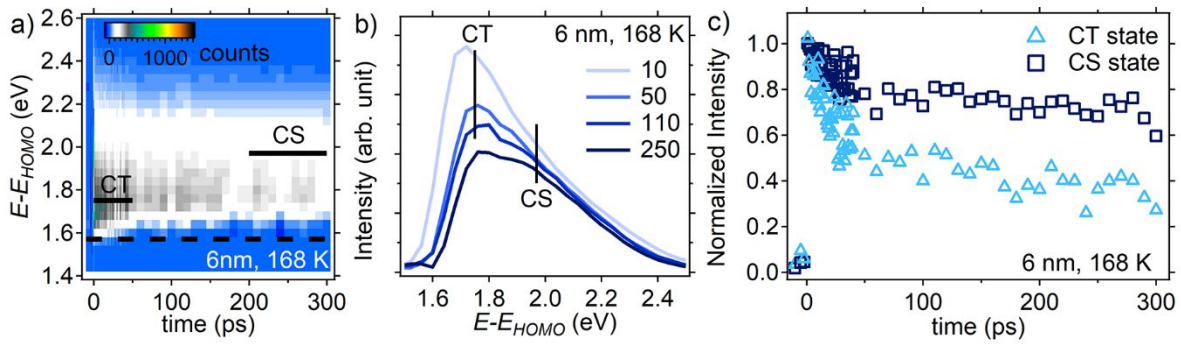

Figure 3: a) The TR-TPPE spectrum of the 6-nm F_8ZnPc/ML-WS_2 sample collected at 168 K. No apparent shift of the peak towards high energies is observed. b) The spectra at various delay times (indicated on the legend). c) The normalized intensity at energies corresponding to the CT and CS peaks as a function of time.

The entropy driving force should decrease at lower temperatures. This contrasts with hot exciton dissociation mechanisms which are typically temperature independent.[34] We have performed the measurement on the 6-nm sample at a lower temperature. Figure 3a shows the TR-TPPE spectrum obtained at 168 K. No apparent spectral shift towards higher energies is observed, which indicates that CT exciton dissociation is largely suppressed at lower temperatures. A side-

by-side comparison of spectra collected at room temperature and at 168 K is provided in Fig. S4 in the ESI. It is clear from the comparison that the spectral weight is shifted from the lower energy CT state to the higher energy CS state at room temperature, but not at 168 K. This observation is consistent with the decrease in the entropy-driving force at low temperatures. Figure 3b shows the spectra at different times. The intensity decreases with increasing time across the whole spectral range. However, the intensity near the CS peak decreases at a slower rate and a shoulder corresponds to the CS state emerges at long delay times (250 ps). Apparently, some separated electrons (CS state) are still presence, but they are not generated from the CT excitons. Similar to the observation at the room temperature, we believe that some free carriers are generated at early time (~ 1 ps or below) through hot mechanisms.[34] The normalized intensity for the two states is shown in Fig. 3c. To explain the observed dynamics, we note that the CS state should have a longer lifetime compared to the CT state because of a larger spatial separation between the electron and the hole. This leads to a slower intensity decay rate for the CS state as compared to the CT state.

Results from an even thicker F_8ZnPc film provide further evidence that free carriers are generated spontaneously from the interface. Figure 4a shows the TR-TPPE spectrum for 15 nm F_8ZnPc/WS_2 measured at room temperature. At this thickness, because the photoemission probe is surface sensitive, it can no longer probe the CT state with its electron residing near the buried interface. Nevertheless, as shown in Fig. 4c, the intensity at energies corresponding to the CS state increases gradually throughout the time window assessable by our setup (up to 300 ps). Because the photoemission signal is originated from electrons near the surface of the F_8ZnPc layer, the gradual increase in the signal can be attributed to the diffusion of free electrons, generated from the dissociation of the CT exciton, from the buried interface to the sample surface. We note that there is a two-step increase in the signal. The rapid increase at $t < 50$ ps and the slow increase at t

> 50 ps can be attributed to free charges generated from the fast hot CT exciton dissociation[34] and the slower enthalpy-uphill exciton dissociation, respectively.

As a control experiment, we have also performed the TPPE measurement on a 15 nm F_8ZnPc/graphite sample. The TR-TPPE spectrum for this sample is shown in Fig. 4c. As we discussed earlier, the large work function of thick F_8ZnPc prohibits us from capturing the full S_1 peak, but the high energy tail of the F_8ZnPc S_1 peak can still be captured in the spectrum, which is populated immediately after the pump-excitation. Unlike WS_2, graphite is a conductor. Hence, it will quench the F_8ZnPc S_1 exciton produced by the pump pulse instead of splitting the S_1 exciton into an electron-hole pair. No free electrons should be generated from such interface. Indeed, we do not observe a peak or a shoulder at the energy corresponding to the CS state (the horizontal bar in Fig. 4c). For comparison, the normalized intensity at the energy window corresponding to the CS state for the F_8ZnPc/graphite sample is also plotted in Fig. 4b. We observe a monotonic decrease in the photoemission signal, which is consistent with S_1 exciton quenching instead of free carrier generation.

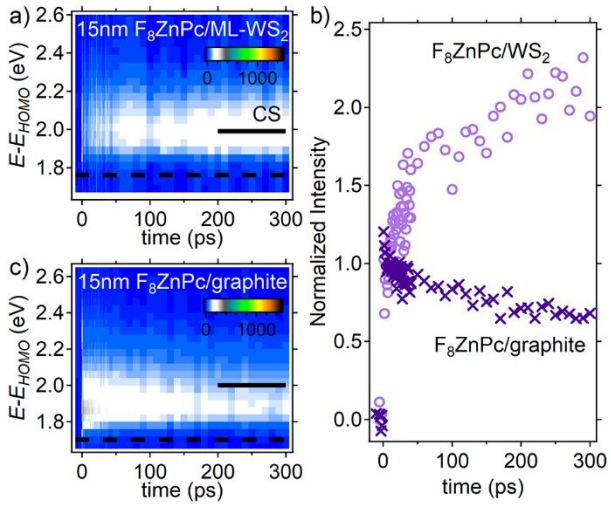

Figure 4: a) The TR-TPPE spectra for the a) 15-nm F_8ZnPC/ML-WS_2, and b) 15-nm F_8ZnPC/graphite collected at the room temperature. c) The normalized intensity at the CS peak energy for the two samples as a function of time.

Finally, we comment on why the entropy-driven dissociation can occur at organic/2D interfaces. As we mentioned earlier, F_8ZnPc deposited on WS_2 has a face-on orientation. Hence, the π-stacking direction in the organic film is perpendicular to the interface, which allows the electron in the F_8ZnPc film to delocalize in the out-of-plane direction (Fig. 1a). For our previous works on organic/organic heterostructures,[30, 31, 58] the electron delocalization size in similar small molecules is ~ 4 nm. The out-of-plane delocalization means that the electron is localized in the in-plane direction even though the film is continuous. Because the hole in WS_2 is delocalized in the in-plane direction. The orthogonally oriented electron and hole wavefunctions within the CT exciton minimize the contact area between them. As we have shown previously in our works on organic/organic heterostructures, a minimal contact area between the delocalized electron and hole wave function can favor the entropy-driven dissociation process.[30, 40] Indeed, many π-conjugated molecules have a face-on orientation on TMDC,[61] which means that CT exciton dissociation can be rather effective in most organic/2D interfaces.

Concluding remark

In conclusion, we observed an enthalpy uphill CT exciton dissociation process occurs at the F_8ZnPc/WS_2 interface in which the CT exciton spontaneously gains an energy of ~0.25 eV in ~ 50 ps. We attribute the observed enthalpy uphill process to entropy-driven charge separation. This observation can explain why CT excitons at organic/TMDC can dissociate effectively despite its large binding energy. Moreover, an entropy-driven CT exciton dissociation process can have an important implication on the free carrier lifetime. Kinetically, while the entropy driving force drives the CT exciton dissociation, it acts as a free energy barrier for the reverse process. Hence, free electrons and holes are much less likely to convert back to bound CT excitons, which can lead to a very long free carrier lifetime. In the extreme case where the entropic driving force is larger

than the CT exciton binding energy, the conversion from the CS state to the CT state can increase the free energy and becomes thermodynamically unfavorable. Essentially, an electron and a hole will "repel" each other at such interface, which can significantly suppress carrier recombination.

The entropy-driven process is favorable when the delocalized electron and hole wave functions within the CT exciton has a minimal spatial contact.[30, 40] This condition is fulfilled in many small molecules/TMDC interfaces because molecules typically has a face-on orientation on TMDCs, which makes the π-stacking direction perpendicular to the interface. Therefore, organic/TMDC heterostructures can be a favorable materials system for photo-to-electrical energy conversion applications.

Experimental section

Sample preparation. Continuous CVD-grown ML-WS_2 was purchased from a commercial vendor (6Carbon Technology, China). The ML-WS_2 was transferred on a naïve oxide/Si (high doped) substrate by the vendor. From the characterization data provided by the vendor (www.6carbon.com), the grain size is in the range of 50 – 150 μm, and the monolayer coverage is over 95 %. After the sample was loaded into our UHV system, the sample was heated at 400 – 450 °C for ~30 hours in the photoemission chamber with a base pressure of 8×10^{-11} Torr. Once a clear ARPES spectrum was obtained, the sample was transferred to a deposition chamber with a base pressure of 1×10^{-9} Torr. F_8ZnPc molecules (Luminescence Technology, >99%) was thermally evaporated onto the WS_2 at room temperature. For thicknesses up to 2 nm, a substrate temperature of 90 °C and a deposition rate of 0.3 Å/min were used. For larger thicknesses, the deposition rate was increased to 0.8 Å/min and the sample was kept at room temperature. The thickness of the F_8ZnPc was monitored using a quartz crystal microbalance. After the deposition,

the sample was transferred back to the photoemission chamber where the photoemission experiments were performed.

ARPES/UPS experiment. A standard UV lamp was used to produce the UV light for the UPS measurement. The He-I emission line having 21.22 eV photon energy was used for our experiment. For ARPES measurement, the energy and angle of emission of the photoelectrons were resolved with a hemispherical analyzer equipped with an imaging detector (Phoibos 100, SPECS). For UPS measurements, photoelectrons emitted along the surface normal direction were collected. For the bare-WS_2 sample, we notice some slow sample charging during the UPS/ARPES measurement as the whole spectrum shifted slowly towards lower energies) when the sample was illuminated by the UV light (ESI, Fig. S8). In this case, we used the spectrum collected immediately after the UV light was turned on. No apparent sample charging was observed after the sample was covered by F_8ZnPc.

TR-TPPE spectroscopy. TR-TPPE spectroscopy was used to measure the energy and population of excited electrons in the sample. The sample was excited by 25-fs pump pulses with its central wavelength kept at ~700 nm. For the photoemission probe, 65-fs probe pulses with a wavelength of 270 nm were used to ionize the excited electron. The kinetic energy of photoelectrons was measured with the same hemispherical analyzer used for ARPES/UPS. The pump and probe beams were generated by using the outputs of two noncollinear optical parametric amplifiers (Orpheus-2H and Orpheus-3H, Light Conversion), which were pumped by a Yb:KGW regenerative amplifier running at 125 kHz (Pharos - 10 W, Light Conversion). The 270 nm probe pulses were generated by frequency doubling the Orpheus-3H output. Both beams had a full-width half-maximum (fwhm) size of 1.0 mm at the sample. All experiments were done at room temperature unless otherwise stated. The incidence fluence for the pump pulse is ~ 25 $\mu J\ cm^{-2}$

unless otherwise stated. The excitation density for the 6-nm F_8ZnPc film is estimated to be ~ 6×10^{12} cm^{-2} by assuming ~7 % of the incident fluence is absorbed.[62] The incidence fluence for the probe pulse is in the range of 1.1 – 0.5 μJ cm^{-2}, which is much smaller than that of the pump pulse.

Acknowledgement:

This material is based upon work supported by the U.S. Department of Energy, Office of Science, Office of Basic Energy Sciences, Chemical Sciences, Geosciences, and Biosciences Division under Award Number DE-SC0024525. W. L. C. also acknowledges the support from the University of Kansas General Research Fund allocation #2151080. F.R. acknowledges the scholarship support from Jazan University.

Reference:

1. K. S. Novoselov, A. Mishchenko, A. Carvalho and A. H. C. Neto, *Science*, 2016, **353**, 461.
2. W. J. Zhang, Q. X. Wang, Y. Chen, Z. Wang and A. T. S. Wee, *2D Mater.*, 2016, **3**, 022001.
3. S. Das, J. A. Robinson, M. Dubey, H. Terrones and M. Terrones, *Annu. Rev. Mater. Res.*, 2015, **45**, 1-27.
4. D. Jariwala, T. J. Marks and M. C. Hersam, *Nat. Mater.*, 2017, **16**, 170-181.
5. Y. L. Huang, Y. J. Zheng, Z. B. Song, D. Z. Chi, A. T. S. Wee and S. Y. Quek, *Chem. Soc. Rev.*, 2018, **47**, 3241-3264.
6. M. Gobbi, E. Orgiu and P. Samori, *Adv. Mater.*, 2018, **30**, 1706103.
7. S. Velez, D. Ciudad, J. Island, M. Buscema, O. Txoperena, S. Parui, G. A. Steele, F. Casanova, H. S. J. van der Zant, A. Castellanos-Gomez and L. E. Hueso, *Nanoscale*, 2015, **7**, 15442-15449.
8. F. C. Liu, W. L. Chow, X. X. He, P. Hu, S. J. Zheng, X. L. Wang, J. D. Zhou, Q. D. Fu, W. Fu, P. Yu, Q. S. Zeng, H. J. Fan, B. K. Tay, C. Kloc and Z. Liu, *Adv. Funct. Mater.*, 2015, **25**, 5865-5871.
9. J. Pak, J. Jang, K. Cho, T. Y. Kim, J. K. Kim, Y. Song, W. K. Hong, M. Min, H. Leec and T. Lee, *Nanoscale*, 2015, **7**, 18780-18788.
10. D. Jariwala, S. L. Howell, K. S. Chen, J. M. Kang, V. K. Sangwan, S. A. Filippone, R. Turrisi, T. J. Marks, L. J. Lauhon and M. C. Hersam, *Nano Lett.*, 2016, **16**, 497-503.
11. X. Liu, J. Gu, K. Ding, D. J. Fan, X. E. Hu, Y. W. Tseng, Y. H. Lee, V. Menon and S. R. Forrest, *Nano Lett.*, 2017, **17**, 3176-3181.
12. Y. Huang, F. W. Zhuge, J. X. Hou, L. Lv, P. Luo, N. Zhou, L. Gan and T. Y. Zhai, *ACS Nano*, 2018, **12**, 4062-4073.
13. H. M. Li, D. Lee, D. S. Qu, X. C. Liu, J. J. Ryu, A. Seabaugh and W. J. Yoo, *Nat. Commun.*, 2015, **6**, 6564.

14. J. H. Park, A. Sanne, Y. Z. Guo, M. Amani, K. H. Zhang, H. C. P. Movva, J. A. Robinson, A. Javey, J. Robertson, S. K. Banerjee and A. C. Kummel, *Sci. Adv.*, 2017, **3**, 1701661.
15. S. Park, N. Mutz, S. A. Kovalenko, T. Schultz, D. Shin, A. Aljarb, L. J. Li, V. Tung, P. Amsalem, E. J. W. List-Kratochvil, J. Stahler, X. M. Xu, S. Blumstengel and N. Koch, *Adv. Sci.*, 2021, **8**, 2100215.
16. L. Ye, X. H. Xu, S. Y. He, Y. P. Liu, Y. Z. Jin, Y. M. Yang and H. M. Zhu, *ACS Nano*, 2022, **16**, 12532-12540.
17. K. Rijal, S. Amos, P. Valencia-Acuna, F. Rudayni, N. Fuller, H. Zhao, H. Peelaers and W. L. Chan, *ACS Nano*, 2023, **17**, 7775-7786.
18. K. Ulman and S. Y. Quek, *Nano Lett.*, 2021, **21**, 8888-8894.
19. R. Canton-Vitoria, H. B. Gobeze, V. M. Blas-Ferrando, J. Ortiz, Y. Jang, F. Fernández-Lázaro, Á. Sastre-Santos, Y. Nakanishi, H. Shinohara, F. D'Souza and N. Tagmatarchis, *Angew. Chem. Int. Ed.*, 2019, **131**, 5768-5773.
20. X. P. Hong, J. Kim, S. F. Shi, Y. Zhang, C. H. Jin, Y. H. Sun, S. Tongay, J. Q. Wu, Y. F. Zhang and F. Wang, *Nat. Nanotechnol.*, 2014, **9**, 682-686.
21. F. Ceballos, M. Z. Bellus, H. Y. Chiu and H. Zhao, *ACS Nano*, 2014, **8**, 12717-12724.
22. P. Rivera, J. R. Schaibley, A. M. Jones, J. S. Ross, S. F. Wu, G. Aivazian, P. Klement, K. Seyler, G. Clark, N. J. Ghimire, J. Q. Yan, D. G. Mandrus, W. Yao and X. D. Xu, *Nat. Commun.*, 2015, **6**, 6242.
23. J. L. Bredas, J. E. Norton, J. Cornil and V. Coropceanu, *Acc. Chem. Res.*, 2009, **42**, 1691-1699.
24. T. M. Clarke and J. R. Durrant, *Chem. Rev.*, 2010, **110**, 6736-6767.
25. J. Z. Yao, T. Kirchartz, M. S. Vezie, M. A. Faist, W. Gong, Z. C. He, H. B. Wu, J. Troughton, T. Watson, D. Bryant and J. Nelson, *Phys. Rev. Appl.*, 2015, **4**, 014020.
26. B. P. Rand, D. P. Burk and S. R. Forrest, *Phys. Rev. B*, 2007, **75**, 115327.
27. S. Padgaonkar, S. H. Amsterdam, H. Bergeron, K. Su, T. J. Marks, M. C. Hersam and E. A. Weiss, *J. Phys. Chem. C*, 2019, **123**, 13337-13343.
28. C. M. Zhong, V. K. Sangwan, C. Wang, H. Bergeron, M. C. Hersam and E. A. Weiss, *J. Phys. Chem. Lett.*, 2018, **9**, 2484-2491.
29. S. B. Homan, V. K. Sangwan, I. Balla, H. Bergeron, E. A. Weiss and M. C. Hersam, *Nano Lett.*, 2017, **17**, 164-169.
30. T. R. Kafle, B. Kattel, S. Wanigasekara, T. Wang and W. L. Chan, *Adv Energy Mater*, 2020, **10**, 1904013.
31. T. Wang, T. R. Kafle, B. Kattel and W.-L. Chan, *Journal of the American Chemical Society*, 2017, **139**, 4098-4106.
32. P. Valencia-Acuna, F. Rudayni, K. Rijal, W. L. Chan and H. Zhao, *ACS Nano*, 2023, **17**, 3939-3947.
33. K. Greulich, A. Belser, S. Bölke, P. Grüninger, R. Karstens, M. S. Sättele, R. Ovsyannikov, E. Giangrisostomi, T. V. Basova, D. Klyamer, T. Chassé and H. Peisert, *J. Phys. Chem. C*, 2020, **124**, 16990-16999.
34. Z. K. Wang, C. Sun, X. H. Xu, Y. P. Liu, Z. Chen, Y. Yang and H. M. Zhu, *J. Am. Chem. Soc.*, 2023, **145**, 11227-11235.
35. T. R. Kafle, B. Kattel, P. Yao, P. Zereshki, H. Zhao and W. L. Chan, *Journal of the American Chemical Society*, 2019, **141**, 11328-11336.

36. P. Westacott, J. R. Tumbleston, S. Shoaee, S. Fearn, J. H. Bannock, J. B. Gilchrist, S. Heutz, J. deMello, M. Heeney, H. Ade, J. Durrant, D. S. McPhail and N. Stingelin, *Energy Environ Sci*, 2013, **6**, 2756-2764.
37. T. M. Burke and M. D. McGehee, *Adv. Mater.*, 2014, **26**, 1923-1928.
38. L. Shi, C. K. Lee and A. P. Willard, *Acs Central Sci*, 2017, **3**, 1262-1270.
39. R. Wallauer, J. Reimann, N. Armbrust, J. Gudde and U. Hofer, *Appl. Phys. Lett.*, 2016, **109**, 162102.
40. T. R. Kafle and W. L. Chan, *Phys. Rev. Appl.*, 2021, **15**, 044054.
41. H. Henck, Z. Ben Aziza, D. Pierucci, F. Laourine, F. Reale, P. Palczynski, J. Chaste, M. G. Silly, F. Bertran, P. Le Fevre, E. Lhuillier, T. Wakamura, C. Mattevi, J. E. Rault, M. Calandra and A. Ouerghi, *Phys. Rev. B*, 2018, **97**, 155421.
42. S. Duhm, G. Heimel, I. Salzmann, H. Glowatzki, R. L. Johnson, A. Vollmer, J. P. Rabe and N. Koch, *Nat. Mater.*, 2008, **7**, 326-332.
43. W. Chen, H. Huang, S. Chen, Y. L. Huang, X. Y. Gao and A. T. S. Wee, *Chem. Mater.*, 2008, **20**, 7017-7021.
44. T. Wang, T. R. Kafle, B. Kattel, Q. F. Liu, J. Wu and W. L. Chan, *Sci. Rep.*, 2016, **6**, 28895.
45. M. Schwarze, K. S. Schellhammer, K. Ortstein, J. Benduhn, C. Gaul, A. Hinderhofer, L. P. Toro, R. Scholz, J. Kublitski, S. Roland, M. Lau, C. Poelking, D. Andrienko, G. Cuniberti, F. Schreiber, D. Neher, K. Vandewal, F. Ortmann and K. Leo, *Nat. Commun.*, 2019, **10**, 2466.
46. K. K. Okudaira, H. Setoyama, H. Yagi, K. Mase, S. Kera, A. Kahn and N. Ueno, *J. Electron. Spectrosc. Relat. Phenom.*, 2004, **137**, 137-140.
47. W. T. Hsu, J. M. Quan, C. Y. Wang, L. S. Lu, M. Campbell, W. H. Chang, L. J. Li, X. Q. Li and C. K. Shih, *2D Mater.*, 2019, **6**, 025028.
48. W. Y. Gao and A. Kahn, *Org. Electron.*, 2002, **3**, 53-63.
49. D. R. T. Zahn, G. N. Gavrila and M. Gorgoi, *Chem. Phys.*, 2006, **325**, 99-112.
50. I. G. Hill, A. Kahn, Z. G. Soos and R. A. Pascal, *Chem. Phys. Lett.*, 2000, **327**, 181-188.
51. X. C. He, G. B. Zhu, J. B. Yang, H. Chang, Q. Y. Meng, H. W. Zhao, X. Zhou, S. Yue, Z. Wang, J. A. Shi, L. Gu, D. H. Yan and Y. X. Weng, *Sci. Rep.*, 2015, **5**, 17076.
52. T. Wang and W. L. Chan, *J. Phys. Chem. Lett.*, 2014, **5**, 1812-1818.
53. S. Neppl, A. Shavorskiy, I. Zegkinoglou, M. Fraund, D. S. Slaughter, T. Troy, M. P. Ziemkiewicz, M. Ahmed, S. Gul, B. Rude, J. Z. Zhang, A. S. Tremsin, P.-A. Glans, Y.-S. Liu, C. H. Wu, J. Guo, M. Salmeron, H. Bluhm and O. Gessner, *Faraday Discuss.*, 2014, **171**, 219-241.
54. M. Ogawa, S. Yamamoto, R. Yukawa, R. Hobara, C. H. Lin, R. Y. Liu, S. J. Tang and I. Matsuda, *Phys. Rev. B*, 2013, **87**, 235308.
55. Y. Zhang, D. T. Payne, C. L. Pang, C. Cacho, R. T. Chapman, E. Springate, H. H. Fielding and G. Thornton, *J. Phys. Chem. Lett.*, 2019, **10**, 5265-5270.
56. D. Wegkamp, M. Meyer, C. Richter, M. Wolf and J. Stahler, *Appl. Phys. Lett.*, 2013, **103**, 151603.
57. A. E. Jailaubekov, A. P. Willard, J. R. Tritsch, W. L. Chan, N. Sai, R. Gearba, L. G. Kaake, K. J. Williams, K. Leung, P. J. Rossky and X. Y. Zhu, *Nat. Mater.*, 2013, **12**, 66-73.
58. T. R. Kafle, B. Kattel, T. Wang and W.-L. Chan, *J. Phys.: Condens. Matter*, 2018, **30**, 454001.

59. T. R. Kafle, T. Wang, B. Kattel, Q. Liu, Y. Gong, J. Wu and W.-L. Chan, *J. Phys. Chem. C*, 2016, **120**, 24482-24490.
60. L. Miaja-Avila, J. R. Tritsch, A. Wolcott, W. L. Chan, C. A. Nelson and X. Y. Zhu, *Nano Lett.*, 2012, **12**, 1588-1591.
61. S. H. Amsterdam, T. J. Marks and M. C. Hersam, *J. Phys. Chem. Lett.*, 2021, **12**, 4543-4557.
62. B. Kattel, L. Qin, T. R. Kafle and W. L. Chan, *J. Phys. Chem. Lett.*, 2018, **9**, 1633-1641.